Microstructure – Properties relationship in laser-welded AZ31B magnesium alloy

Maroš Vyskoč [a], Mirjana Novaković [b], Jelena Potočnik [b], Pavel Kovačocy [c], Peter Jurči [d,*]

[a] *Advanced Technologies Research Institute, Faculty of Materials Science and Technology in Trnava, Slovak University of Technology, Jána Bottu 25, 917 24 Trnava, Slovak Republic*
[b] *Department of Atomic Physics, Vinča Institute of Nuclear Sciences - National Institute of the Republic of Serbia, University of Belgrade, 1 Studentski trg, 11000 Belgrade, Serbia*
[c] *Institute of Production Technologies, Faculty of Materials Science and Technology in Trnava, Slovak University of Technology, Jána Bottu 25, 917 24 Trnava, Slovak Republic*
[d] *Institute of Materials Science, Faculty of Materials Science and Technology in Trnava, Slovak University of Technology, Jána Bottu 25, 917 24 Trnava, Slovak Republic*

ARTICLE INFO

ABSTRACT

The AZ31B magnesium alloy was laser-welded at three different (1.2, 1.6, and 2 kW) laser output powers in the present work. All the butt weld joints are almost defect-free. The size of the weld joint slightly increases with increasing laser output power. The weld metal is formed by columnar grains of the alpha phase at the weld metal/base metal interface, but a finely equiaxed grain microstructure is formed in the centres of fusion zones. The minor phases are $Mg_{17}Al_{12}$ and $(Al,Mg)_8Mn_5$. The weld metal microstructure manifests clear refinement with a decrease in laser output power. Microstructural changes are reflected in changes in mechanical properties; weld joints prepared at the lowest laser output power manifest the highest microhardness, ultimate tensile strength, yield strength, and almost 90% joint efficiency. This is related to the different extents of strengthening mechanisms that act most effectively in weld joints made at 1.2 kW laser output power. Detail analysis of fracture surfaces confirmed that lower laser output power and general microstructural refinement favours the formation of plastically deformed material, which is in excellent agreement with both the experimentally determined and the calculated values of yield strength.

1. Introduction

Magnesium alloys are widespread construction materials due to their high strength-to-specific density ratio. As the lightest structural materials, they are often used in various industries, e.g. in aerospace, automotive, and electronics. Among these materials, the non-heat-treatable alloys alloyed with Al and Zn (AZ class) are of great importance. The microstructure of these alloys consists of a Mg-based hexagonal alpha solid solution and an intermetallic phase of $Mg_{17}Al_{12}$ [1–3]. In wrought AZ-class alloys, the matrix consists of equiaxed grains; the $Mg_{17}Al_{12}$ phase particles are located at the grain boundaries as a result of their segregation during solidification [4].

Over the last decade, great attention has been paid to the welding of magnesium alloys because of the gradually increasing use of lightweight metals in a variety of industrial branches. However, their unfavourable physical and chemical properties, such as low boiling temperature, high vapour pressure, and large solidification shrinkage, make serious obstacles in fusion welding such as unstable weld pools, underfill, excess root penetration, loss of alloying elements, excessive porosity, and large distortion [5]. As an alternative method to the fusion welding techniques of Mg-alloys, explosive welding has been established [6]. This welding method can overcome the problems associated with the solidification of Mg alloys; however, its suitability for welding of different components is limited. Another way to reduce the undesirable effects of unfavourable metallurgical characteristics of Mg alloys on the quality of weld joints is to minimize the size of the weld pool. The use of laser beam welding (LBW) offers to reduce the volume of molten metal to a very low level; moreover, it is possible to carefully control the processing parameters influencing process stability and reproducibility to reliably produce defect-free welds [5].

The quality of the obtained laser weld joints is governed by the welding parameters and thereby, by the presence of defects as well as by

the resulting weld's microstructures. If too low laser power density is used, for instance, then macro defects like undercuts or low penetration can be encountered in weld joints [4,5,7]. The excessive heat input, on the other hand, may lead to the burning loss of magnesium and alloying elements, which results in an incompletely filled groove [4]. The use of appropriate filler metal (in the form of wire) can effectively compensate for these metal losses [8]. Besides that, the filler metals reduce burn-up and weld drop-through and reduce the porosity of joints. To obtain a stable welding process and accepted weld quality (without macro-defects), a balance between laser output power, welding speed, focusing, and other parameters must be thoroughly chosen. Internal porosity is another type of macro-defect that can deteriorate the quality of weld joints. In the welding of Mg alloys, the internal porosity may result from the collapse of unstable keyholes (too deep keyholes are inherently unstable) [9]. Other sources of internal porosity in weld joints of magnesium alloys are turbulent flow of molten metal in the weld pool [5], initial pre-existing pores [5,10], interaction of molten Mg with surrounding air or moisture [11], surface oxide films [5], and contaminants (hydrides, grease/releasing agents, surface coatings, dirt picked up during the forming operation or storage of components) [5,8]. In cast Mg alloys, the extent of internal porosity in weld joints strongly depends on the initial gas porosity in the base material [5,10]. Therefore, it is necessary to reduce the porosity in cast Mg alloys by using vacuum casting, for instance, in order to manufacture well-weldable castings. Some Mg alloys are inherently poorly weldable; one typical reason is the large temperature solidification interval, which makes the alloys sensitive to solidification cracking. The Mg-Zn-Zr or Mg-Al-Zn alloys are the most typical examples [5].

The microstructures of fusion zones of welded magnesium alloys are typical by the presence of columnar crystals of alpha phase, growing perpendicularly to the fusion boundary [7,12–17]. The second microstructural feature that occurs in the centres of the welds is equiaxed grains [13,14,18,19]. A significant refinement of grains occurs in weld metal, as compared with base metals, because of the rapid solidification of molten metal during laser welding, e.g. [7,12,13,18,20]. The minor phase that is present in fusion zones of welded AZ-class Mg alloys as less or more regularly shaped and sub-micron-sized particles is $Mg_{17}Al_{12}$ [12,14,18,21]. Besides, Al_8Mn_5 nano-sized particles were also observed in some investigations [22].

In most cases, the hardness of fusion zones manifests a clear increment as compared with the base metal. Wang et al. [4] and Coelho et al. [23] recorded a 10 HV hardness increase in the fusion zone in comparison with the AZ31B base metal. The welding of AZ31 material by using a Nd:YaG laser gave similar hardness increments [22]. Much more remarkable, an almost 25 HV increase in hardness was found by Zhang et al. [17] by laser welding of the Mg-10Li-3Al-3Zn alloy. Alternatively, a hardness decrease was also recorded in fiber laser-created fusion zones of the AZ31 alloy by Chowdhury et al. [14]. But a plastically deformed alloy was used for welding in this case instead of recrystallized ones utilized in other works.

The recorded ultimate tensile strength (UTS) values make up usually 90–95% of the UTS of the base metals (joint efficiency 90–95%) [4,15,22], at correspondingly lower (by 10–20%) elongation. However, the UTS also depends on the heat input into the materials; higher heat inputs result in lower values of joint efficiency [14,17] since greater weld joints with coarser internal microstructures are formed. An exception was the Mg-10Li-3Al-3Zn alloy, where the joint had the same (or slightly higher) UTS as compared with the base metal [17]. But a slight increase in UTS is accompanied by a 15% sacrifying of elongation. At this place it is also worth noting that, in the latter cited source, the corrosion resistance of the weld joints has also been examined. The obtained results infer that there is no worsening but rather an improvement in the corrosion resistance of weld joints in comparison to the base metal.

Even though many studies on the welding of AZ-class alloys have been published to date and the resulting microstructures, mechanical

Table 1
Chemical composition of the examined AZ31B magnesium alloy (in wt%).

Al	Zn	Mn	Si	Cu	Fe	Ni	Mg
3.06	0.75	≤0.2	0.1	0.05	≤0.005	≤0.005	Balance

Table 2
Mechanical properties of as-delivered sheet made of AZ31B magnesium alloy, as measured by tensile test at the room temperature.

R_m [MPa]	$R_{p0.2}$ [MPa]	A_{50}, [%]	HV
253	201	15	49

Table 3
Chemical composition of filler wire (in wt%).

Al	Zn	Si	Mn	Cu	Ni	Mg
2.65	1.21	0.015	0.24	0.05	0.01	Balance

properties, and formation mechanism of welding defects such as cracks, porosity, element loss, and craters in the welded seams of laser-welded magnesium alloys have been described, the research about the effects of heat input on the interconnection between the microstructures and mechanical properties of weld joints is deficient to our knowledge. Therefore, the effects of laser output input on the microstructures and mechanical properties of laser welded AZ31 magnesium alloy joints are in-depth investigated and discussed in the present work. Moreover, the relationship between the microstructures and mechanical properties is thoroughly described. The obtained results are supplemented with detailed TEM investigations of weld joints as well as with the morphologies of the obtained tensile fractured surfaces. Finally, experimentally determined yield strength magnitudes of weld metals are compared with the calculated ones by considering the obtained microstructures.

2. Experimental
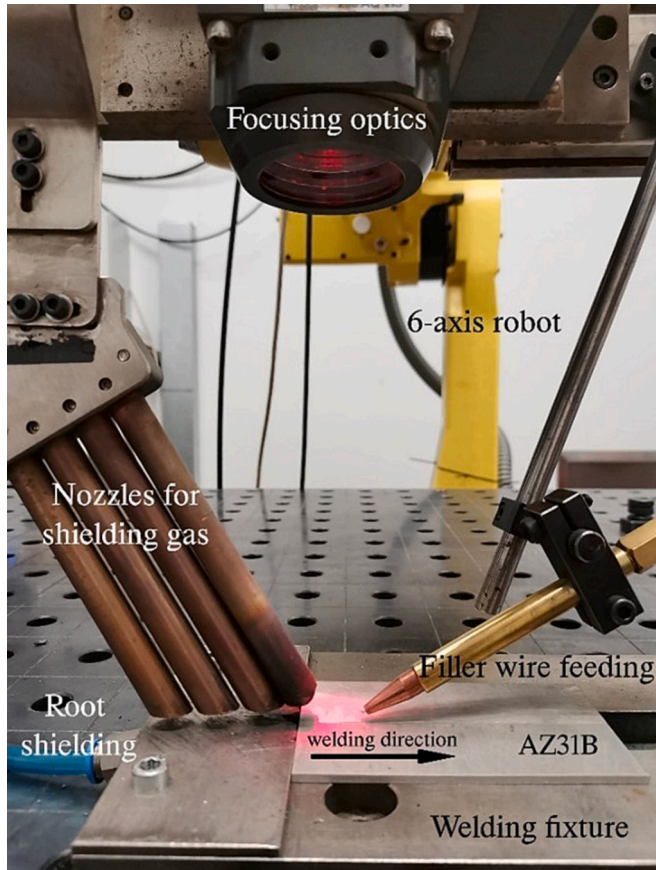
2.1. Characterization of material

In the present study, a 2 mm thick sheet made of AZ31B alloy with the nominal chemical composition in Table 1 was used for investigations. The main mechanical properties of the as-delivered sheet are listed in Table 2. The chemical composition of the filler wire is given in Table 3.

2.2. Laser equipment and welding parameters

Just prior to welding, the specimens were subjected to fine grinding by 600-grit emery paper in order to remove the oxides from the surface. Then, the specimens were cleaned with acetone and dried. Butt-welded joints were done by using a TruDisk 4002 YB:YAG disk laser in continuous-wave mode with a wavelength of 1.03 μm and a maximum power of 4 kW. The diameter of the laser spot was 200 μm, and the divergence of the laser beam was 8 mm.mrad. The whole welding process was controlled by a 6-axis robot M-710iC/50. Argon with a purity of 99.996% was used as a shielding gas to protect the surface and the root of the weld against oxidation. For better protection efficiency a four-tube shielding gas nozzle has been used. This protection was active for further approx. 15 s after forming the weld joint. To compensate for the loss of alloying elements, a filler wire made of AZ31 (composition given in Table 3) with a diameter of 1.2 mm was used. Based on the recent processing optimization [24], the only processing variable in this work was the laser output power, while the other processing parameters were kept constant, Table 4. Fig. 1 shows the experimental setup of the

Table 4
Welding parameters used in the current work.

No.	Laser power [kW]	Welding Speed [mm/s]	Heat input [J/mm]	Wire feed rate [cm/min]	Type of shielding gas	Shielding gas flow rate [l/min]	Focusing [mm]
1	1.2	40	30	110	Ar	30	0
2	1.6	40	40	110	Ar	30	0
3	2.0	40	50	110	Ar	30	0

Fig. 1. Experimental setup for laser welding of AZ 31B alloy in the current work.

Fig. 2. A schematic of the microhardness measurements throughout the laser-welded material.

determination of the contents of the main alloying elements Al and Zn in the matrix has been done using EDS analysis. Thirty randomly located EDS spectra were considered, and the mean values were calculated from the obtained results.

The samples for transmission electron microscopy (TEM) were prepared by the focused ion beam (FIB) technique using a FEI Scios 2 Dual Beam scanning electron microscope. TEM lamellas were prepared in cross-section geometry (lift-out technique), which produces a lamella perpendicular to the bulk sample surface. Transmission electron microscopy and high-resolution TEM (HRTEM) were performed on the FEI Talos F200X device operating at 200 kV with an X-FEG source and point-to-point resolution below 0.24 nm. The micrographs were recorded on a CCD camera with a resolution of 4096 × 4096 pixels using the User Interface software package. The samples were also analysed in scanning transmission (STEM) mode with energy dispersive spectrometry (EDS). The EDS detection system was used to determine the elemental area distribution in nano-sized areas inside the welded metal. The technique

welding process.

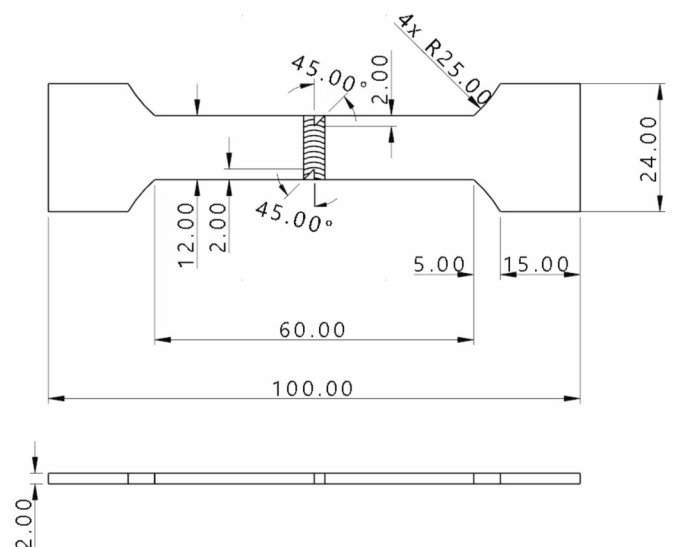### 2.3. Microstructural examinations

The metallographic preparation of samples was performed following the commonly used method: the specimens were first grinded on a set of abrasive emery papers with a grit of 120, 400, 600, and 1200, and then mechanically polished. For structural analyses, cross-sectional samples of weld joints were etched in Picral reagent (100 ml of ethanol and 4.2 g of picric acid) for 12 s. The macro-microstructures were examined using a Neophot 32 light microscope and, for more detailed analysis (and fractography), by using a JEOL 7600F scanning electron microscope (SEM) coupled with electron dispersive spectroscopy (EDS). The grain size was measured following the ČSN EN ISO 643 standard by using ten randomly acquired light micrographs from each characteristic zone of welded sheets. For assessment of the size and interparticle spacings of $Mg_{17}Al_{12}$ particles, twenty randomly acquired SEM micrographs were used; 3000× magnified microstructures were used for interparticle spacing determination, while their size was estimated on 10,000× magnified micrographs. A method by Martinkovic [25] was adopted for both the size- and interparticle spacing determination. The

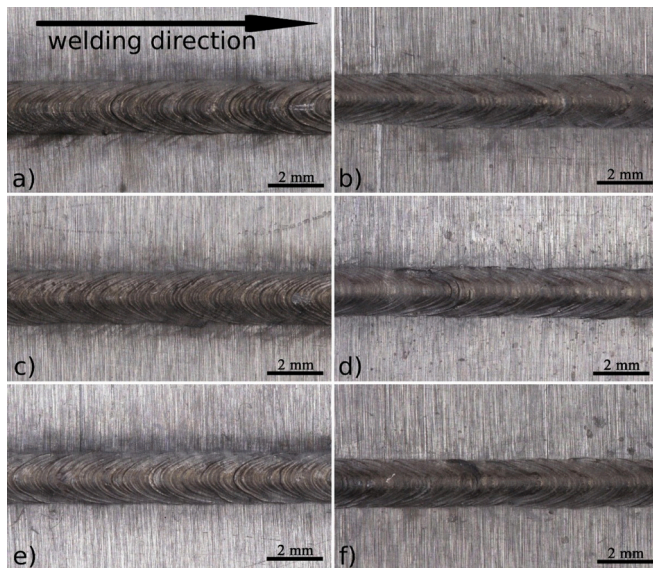**Fig. 3.** A drawing of the tensile test specimen.

Fig. 4. Plan-view light micrographs showing weld beads (images a, c, e) and roots (images b, d, f) produced using the laser power of (a-b) 2.0 kW, (c-d) 1.6 kW, and (e-f) 1.2 kW.
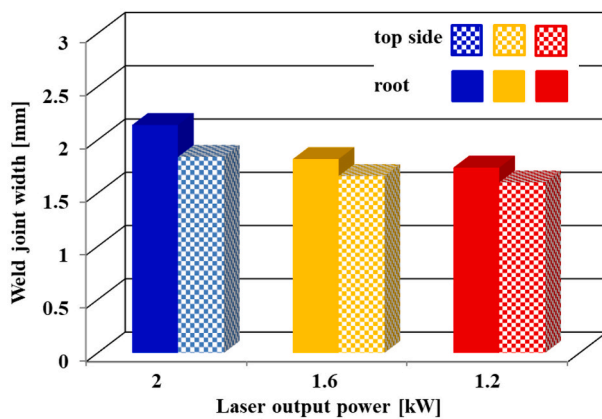

Fig. 5. The effect of laser power on the top side and root weld width.

of high-angle annular dark-field (HAADF) imaging was performed in nanoprobe-TEM mode with probes of below 1 nm size and a camera length of ~205 mm, using the standard annular dark-field detector. In order to determine the nature of minor phases, a selected area diffraction (SAED) technique has been used.

Computed tomography from Zeiss, designated Metrotom 1500, was used to determine the presence of porosity, the distribution of pores in their dimensions and volumes in the weld metal. Metrotom OS 2.8 software was used for scanning, and VG Studio MAX 3.0 software was used to evaluate the results. Welded joints with a length of 100 mm were used to detect pores in the weld metal. The computed tomography scanning parameters were as follows: Filter: Cu 1.5 mm; Number of projections: 2000; Voxel size: 82.57 μm; Voltage: 170 kV; Current: 600 μA; Distance from X-ray lamp: 310 mm; Integration time: 2000 ms; Detector resolution: 1024 × 1024 px. The Buehler IndentaMet 1100 was used to determine the Vickers HV 0.1 (load of 0.98 N) microhardness. According to a schematic in Fig. 2, the distance between two adjacent indents was 200 μm in the base material, but it was reduced to 100 μm. A tensile test of the laser weld specimens has been carried out by using a LabTest 5.250 Sp1machine at the room temperature and with a crosshead speed of 5 mm/s. To ensure the rupture of the specimens inside the weld metal, a notch was created in the weld joints. A drawing of the tensile test specimen is in Fig. 3.

3. Results and discussion

3.1. Welds appearance and macrostructure

Figure 4 shows plan-view images of the top sides and roots of prepared welded joints. The surfaces of the welds are relatively smooth, manifest a regular shape, and are free of spatters, cracks, or undercuts. Fig. 5 shows the effect of laser beam power on the width of the weld joint. It is clear from the image that both the top side and root width decrease with decreasing the laser beam power; the average top side width values were 2.14, 1.82, and 1.74 mm for laser powers of 2, 1.6, and 1.2 kW, respectively. The corresponding average root width values were 1.84, 1.66, and 1.6 mm.

The cross-sections of weld joints created at different laser beam powers are shown in Fig. 6. The samples are all fully penetrated, showing a relatively uniform width of welded seams. All the weld joints manifest fairly narrow weld beads, with almost no distortion, cracks, or drop-through. The joint made at a laser power of 2 kW is almost pore-free, Fig. 6a, while only small porosity can be found in the joints made at 1.2 and 1.6 kW, Figs. 6b, c. Moreover, all the samples manifest a slight excess weld metal on the top surface (0.15–0.22 mm) and excessive root penetration (0.21–0.23 mm). The obtained results infer that the use of welding wire (as a filler) has a beneficial effect on the quality of weld joints. If no filler was used in recent experimental works, e.g. [4,12,15] then the obtained weld joints showed a variety of imperfections, such as craters, undercuts, enhanced porosity, incompletely filled groves or total collapse of the weld. While full penetration, uniform width of welded seams, low internal porosity, and the absence of microcracks are typical features of weld joints produced by using an appropriate filler [14,26].

The internal porosity level of weld joints is far below 1 vol% for all three analysed weld joints, Fig. 7. From the literature review, it follows that increased heat input leads to an increase in the internal porosity of weld joints. Wang et al. [4] have used three values of heat inputs (85.7, 62.5 and 44 J/mm) for laser welding of AZ31 alloy, and the corresponding porosity levels were 10.6, 2.2 and 0.4%. Shen et al. [21] laser-welded the AZ61 alloy, at four heat inputs from the range of 21–33 J/mm, and arrived to the finding that the joint efficiency (UTS of welding joint/base metal) strongly increases with a decrease of heat input. They suggested that pores and craters are generated in the weld seam because of evaporation of Mg and Zn at too high heat inputs (lower welding speeds), and that these defects deteriorate the yield strength of the joints. It is worth noting that no filler metals were used in these two works. However, the porosity can be decreased to values far below 1 vol %, by optimizing the welding parameters (heat input, use of shielding gases, careful preparation of welded metals just prior to welding, use of proper filler metal) [3,4,19,23,27]. In these cases, there was only a marginal or no effect of internal porosity on the ultimate tensile strength of weld joints detected. But the ductility of weld joints was significantly reduced even at very little porosity, which is reflected in the brittle fracture of tensile specimens in the majority of cases [14,19]. It is thus highly desirable to produce almost pore-free weld joints; in this case, the mechanical properties obtained describe the material and are not resulting from weld defects influence [17,22]. In the present work, the material was carefully cleaned before the welding, the weld was well protected against oxidation, and proper filer wire was used. Therefore, the obtained welds do not suffer from a large porosity content, suggesting that the obtained values of mechanical properties will characterize the welded material only.

3.2. Microstructure

The microstructure of the base metal consists of grains of Mg-based α-solid solution and fine particles of the $Mg_{17}Al_{12}$ phase, Fig. 8. The
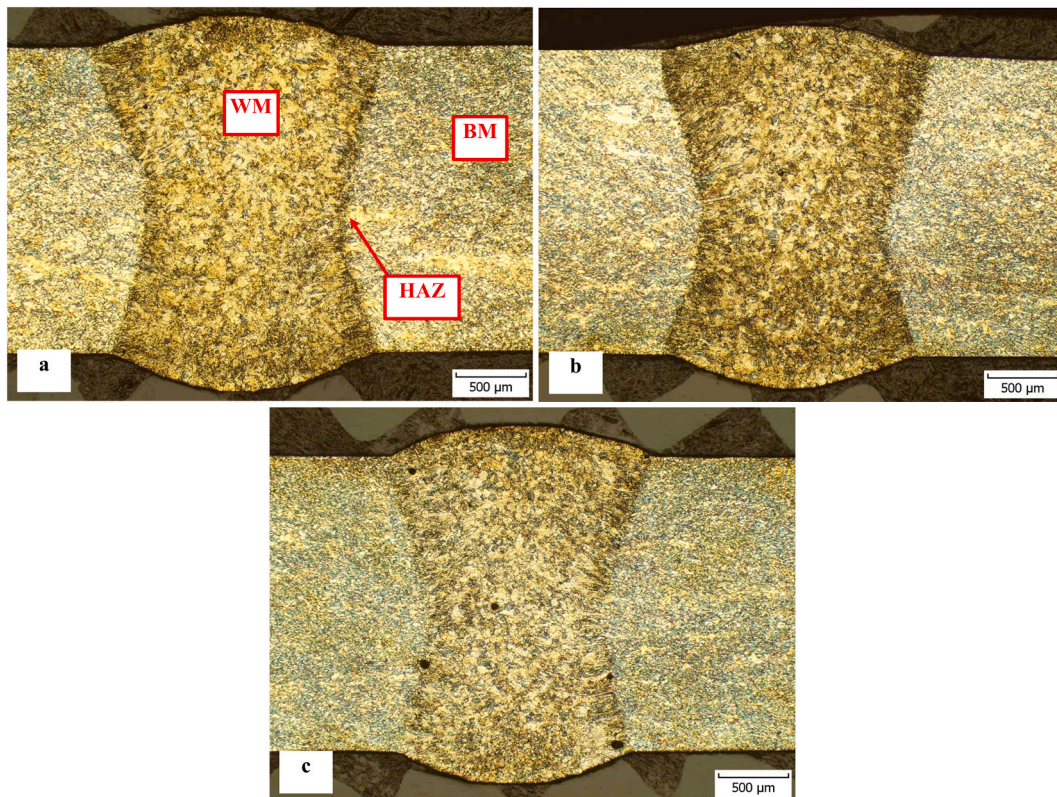
Fig. 6. Cross-sectional light micrographs of the welds made at the laser power of a) 2.0 kW; b) 1.6 kW; c) 1.2 kW. BM: base material; WM: weld metal; HAZ: heat-affected zone (almost invisible at low magnification).
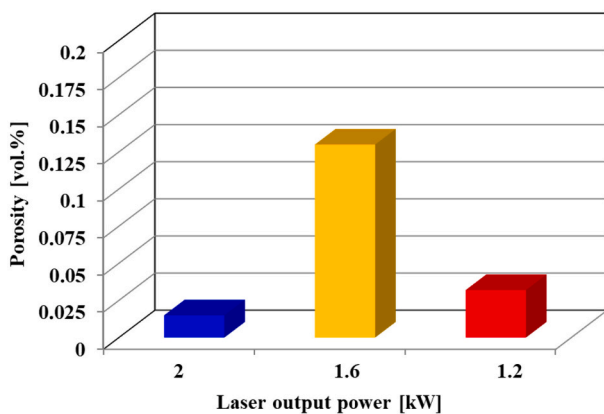

Fig. 7. Internal porosity of weld joints in differently welded samples.

Fig. 8. A light micrograph showing the microstructure of the base material.

average grain size is 32.7 μm.

The microstructures of the BM-WM interface of the welds made at 1.2, 1.6, and 2 kW are shown in Figs. 9a, c, and e. There is only a very narrow (a few tens of μm) heat-affected zone shown on the micrographs. It is typical by slightly coarsened grains, due to the high temperature exposure of the material. Weld metal microstructures adjacent to the fusion lines are mainly columnar, with the direction of less or more ordered grains parallel to the thermal gradient. But the grains are also disordered in some sites, and there are also irregularly-shaped grains visible on the micrographs. The percentage of disordered or irregularly shaped grains cannot be determined exactly; however, it seems that this percentage increases with increasing heat input (or the size of the weld pool). Columnar microstructures are transformed to equiaxed towards the centre of fusion zones, Fig. 9b,d,f. The average values of grain size were determined to be 20.51, 26.37, and 29.59 μm for welds made at
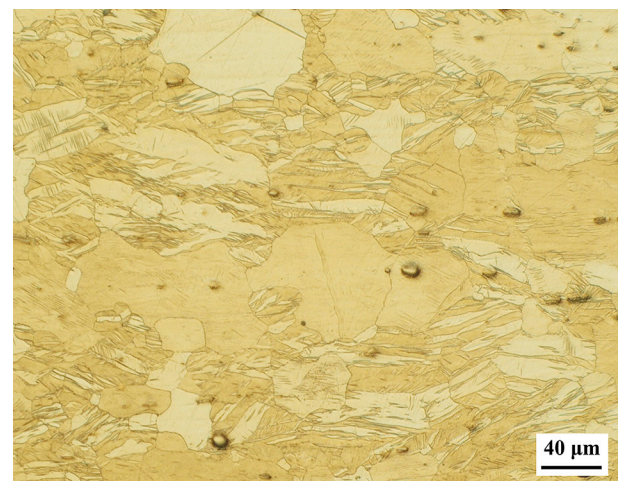
1.2, 1.6, and 2 kW, respectively. Besides the equiaxed alpha-phase grains, the fusion zones exhibited numerous regularly-shaped $Mg_{17}Al_{12}$ particles. These particles are located mainly inside the grains, but some of them are also present at grain boundaries, Fig. 10. In contrast, the base material contains only a very limited number of these particles, see images in Fig. 10a,c, and e. Quantitative metallographic analysis revealed that the mean diameter of the $Mg_{17}Al_{12}$ particles lies around 114 nm and is practically independent on the laser power output within the analysed range. Conversely, the volume fraction and inter-particle spacings of these particles are both strongly influenced by laser output power; the volume fractions were 0.00709, 0.00465 and 0.00379, and the interparticle spacings were 1.5820, 1.8158, and
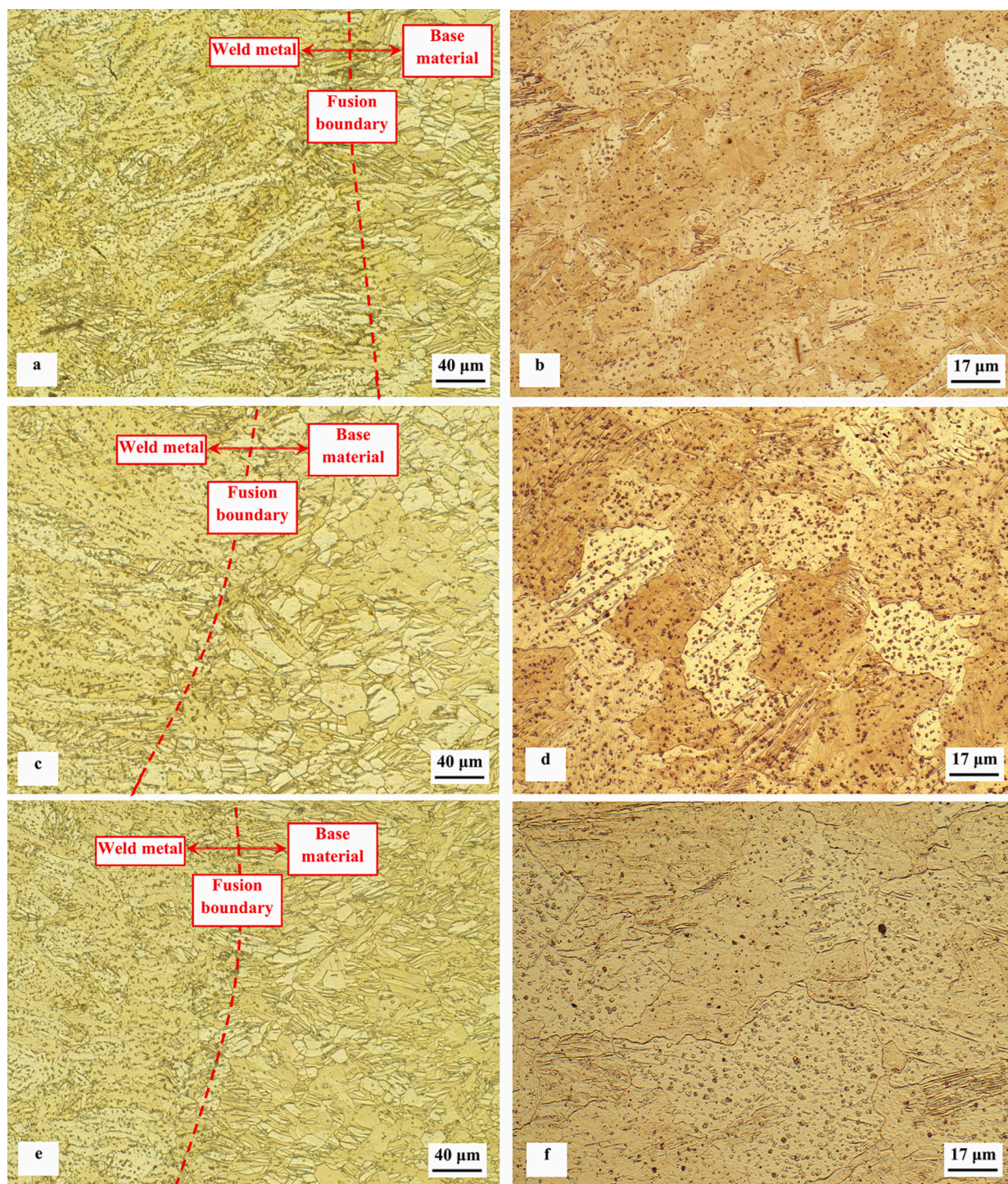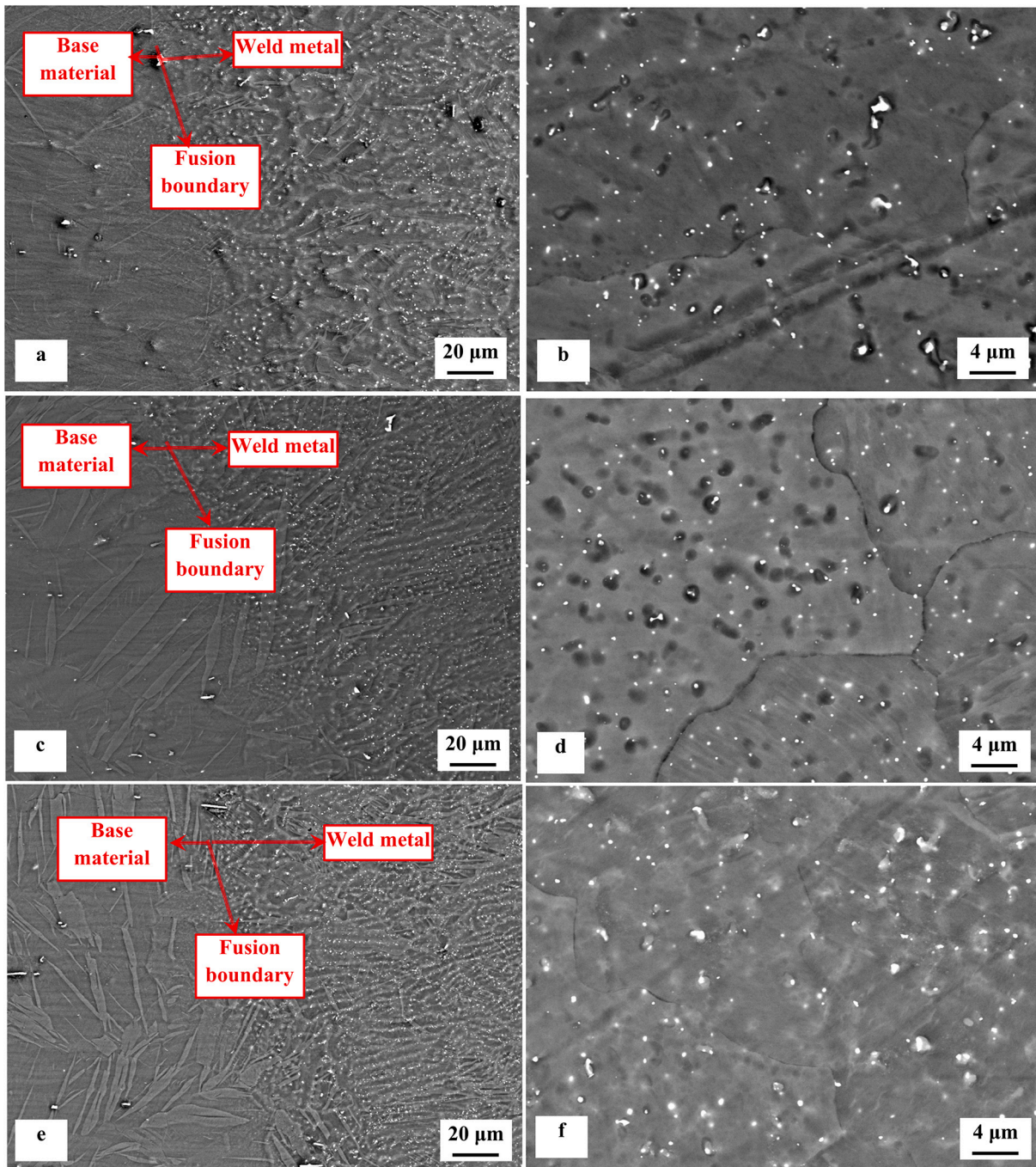
Fig. 9. Light micrographs showing the BM-WM interface of the welds made at 1.2 kW (a), 1.6 kW (c), and 2 kW (e), and the centre of fusion zones of the same welds at 1.2 kW (b), 1.6 kW (d), and 2 kW (f).

1.9502 μm for the output powers of 1.2, 1.6, and 2 kW, respectively. The results of quantitative microstructural analysis as well as the calculated mean values of the main alloying element contents (determined by EDS) are summarized in Table 5.

The obtained weld metal microstructures are typical features of solidified Mg-based metals after fusion welding. Various authors [13,15,23,28–30] have reported the presence of columnar grains in neighbouring fusion lines of weldments made of Mg alloys after either laser- or electron beam welding. The orientation of columnar grains and their ordering can be explained by the generally accepted theory of welding metallurgy: the unmelted base metal acts as the substrate for nucleation and subsequent growth of new grains in the weld pool. These grains grow in a parallel direction but in a reverse orientation to the thermal gradient in the molten and solidifying weld metal. In well-ordered microstructures, some authors also attempted to estimate the changes in size of columnar grains as a function of weld pool size. Chowdhury et al. [14], for instance, indicated that both the length and width of columnar grains increase with heat input (increasing the weld pool size) for the AZ31B-H24 alloy.

The presence of partially disordered or irregularly shaped grains in

Fig. 10. Backscattered scanning electron (BSE) micrographs showing the BM-WM interface of the welds made at 1.2 kW (a), 1.6 kW (c), and 2 kW (e), and the centre of fusion zones of the same welds at 1.2 kW (b), 1.6 kW (d), and 2 kW (f).

the close-to-fusion boundary area is the second aspect that deserves attention. The primary dendrite axes grow from the solid/liquid interface in the direction of the thermal gradient in this area. The solidification then continues with branching the primary dendrites; thus, secondary dendrite arms are formed. If the cooling rate is not high enough then the columnar dendrite may be broken because of the constitutional supercooling of the molten alloy, which can be expressed by Eq. (1).

$$\frac{G}{S_R} \leq \frac{m \times \rho_L}{D} \times \frac{1-K}{K} \tag{1}$$

Where G is the temperature gradient, S_R is the solidification rate, m is the slope of the liquid phase line in the particular phase diagram, ρ_L is

the density of the liquid, D is the diffusion coefficient of the solute, and K is a constant. It implies from Eq. 1 that the lower the G, the larger the constitutional supercooling, and the columnar dendrites are easier to break.

In most cases, the melt becomes more enriched with alloying elements at the root of the secondary dendrite arms. Consequently, the growth at the root is slowed down, and its curvature increases, Fig. 11. The relationship between the curvature at the root and the equilibrium temperature can be expressed by Eq. (2).

$$T - T_0 = -2 \times k \times V_s \times \gamma \times \frac{T_0}{\Delta H_0} \tag{2}$$

where k is the root curvature, T_0 is the equilibrium temperature, V_s is the

Table 5

The results of quantitative microstructural analysis (grain size, parameters of $Mg_{17}Al_{12}$ particles) and calculated mean values of main alloying elements contents (determined by EDS).

Laser output power [kW]	Grain size [μm]	Content of elements in the matrix [at.%]		Parameters of $Mg_{17}Al_{12}$ particles		
		Al	Zn	Volume fraction [−]	Diameter [μm]	Interparticle spacing [μm]
1.2	20.51	2.31	0.32	0.00709	0.11	1.582
1.6	26.37	3.19	0.31	0.00465	0.11	1.816
2	29.59	2.69	0.27	0.00379	0.11	1.950

molar volume in the solid state, ΔH_0 is the standard molar enthalpy, and γ is the interfacial energy. From the equation, it is evident that the larger the root curvature, the lower the equilibrium temperature.

From Eq. 2, it can be deduced that the melting point of the secondary dendrite arm is low at its root because of the large curvature. The dendrites are thus more amenable to breaking at the roots, see Fig. 11. Moreover, convection in the melt pool (which often occurs in laser beam welding) can further promote the columnar dendrite breakdown and their change to the equiaxed grains, by decreasing the thermal gradient.

The presence of equiaxed grains in the centre of fusion zones is also a common feature of laser- or electron beam-welded Mg alloys [4, 12, 13, 15, 21, 23, 26, 28–30]. In the current work, an increase in grain size from 20.51 to 29.59 μm with an increase in laser output power from 1.2 to 2 kW was detected. A similar phenomenon was recorded in some scientific works dealing with laser beam welding of AZ31 [12,14] or AZ61 [21] alloys. It is known that an increase in laser power, at a constant welding speed, will cause an increase in heat input. It is also proven that, as the heat input is increased, the cooling rate within the melt pool decreases during solidification. That is to say, the slower the cooling rate during solidification, the longer the time available for grain growth. Moreover, there is a strong dependency between the nucleation rate I and the degree of supercooling ΔT (which essentially decreases with heat input). This dependency is expressed by Eq. 3:

$$I = I_0 \times exp\left[-\frac{16 \times \pi \times \gamma^3 \times T_0^2}{2\Delta h_m^2 \times k_B \times T} \times \frac{1}{(\Delta T)^2}\right] \qquad (3)$$

where I is the nucleation rate, I_0 is the index factor, γ is the interface energy, Δh_m is the enthalpy per unit volume, k_B is the Boltzmann constant, and ΔT is the supercooling. It is proven that the nucleation rate

increases with the increase in supercooling and vice versa. In the current work, the increase in heat input enlarges the molten pool; thus, the holding time at high temperatures in the weld centre is prolonged, and the solidification rate decreases. Therefore, one can expect that a large number of nuclei are melted again, while only a limited number of nuclei can grow into equiaxed grains of large size due to sufficient growing time.

By visual inspection of the obtained light micrographs from the fusion zone Fig. 9b,d, and f, and by their comparison with the as-cast microstructure of the same alloy (e.g., [31]), it may be concluded that these are solidification microstructures and that the most significant difference between them is in their dispersity. Similar microstructures were obtained by many authors in fusion zones of laser beam [7, 12, 13, 14, 21, 23, 32] or electron beam-welded [30] AZ31 or AZ61 alloys.

The explanation of the presence of great amounts of $Mg_{17}Al_{12}$ in fusion zones as compared with base metal is also an important issue. Chowdhury et al., in their works [14,32], have suggested that the $Mg_{17}Al_{12}$ particles are actually "divorced" eutectic structures and that their presence in the as-welded metal was caused by the fast nonequilibrium cooling of the weld pool during welding. However, they also stated that no normal eutectic structure in the form of alternating layers of alpha-phase and $Mg_{17}Al_{12}$ would be possible in the AZ31 Mg alloy containing only 3 wt% Al based on the equilibrium phase diagram under
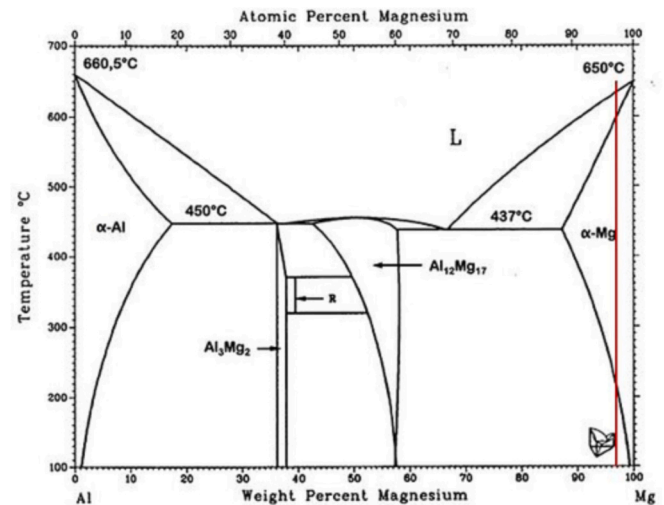
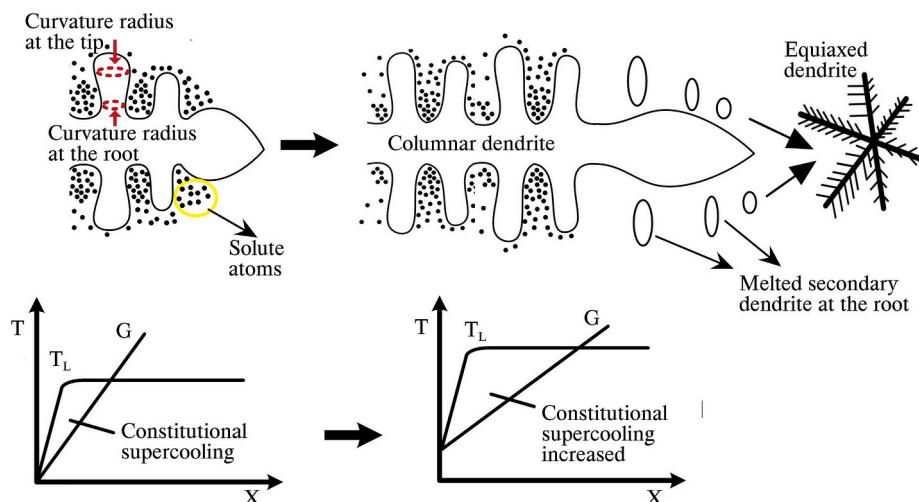**Fig. 12.** The Al—Mg (Aluminium-Magnesium) System [34].

Fig. 11. A schematic of the mechanism of breaking down the columnar dendrite (multiplication of dendrites).
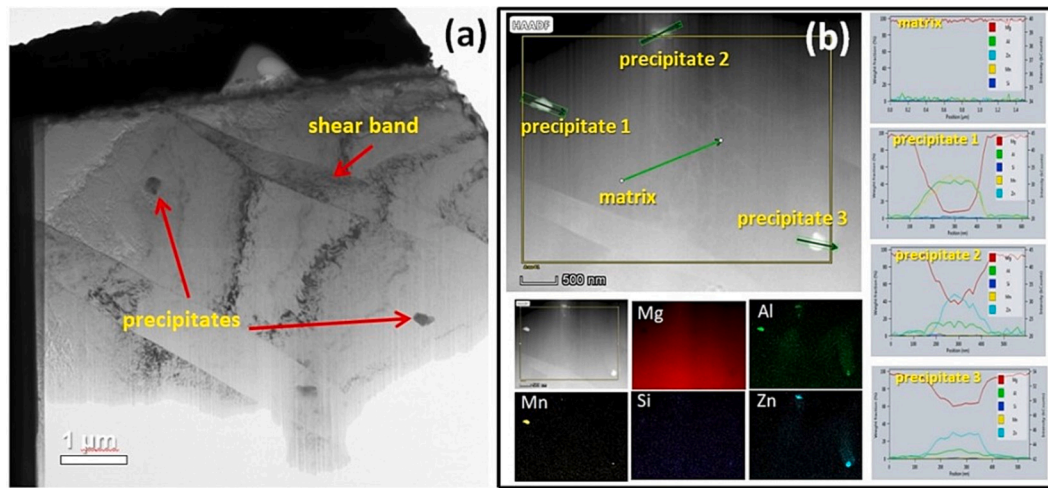
Fig. 13. TEM micrographs showing typical microstructures of weld metal made at 1.2 kW laser power. Bright field overview image (a) and results of STEM/EDS analyses of matrix and precipitates (b).

equilibrium cooling. Therefore, the assumption on "divorced" eutectics seems to be counterintuitive since no eutectic (although "divorced") microstructure can be formed in the given system since the eutectics are formed only at 12.7 wt% Al above [33]. A more reliable concept of the $Mg_{17}Al_{12}$ formation was proposed by Quan et al. [12]. After the laser welding, the melt alloy is rapidly solidified and cooled to room temperature. At the same time, the maximum solid solubility of Al in Mg decreases from 12.7 wt% to about 2.0 wt% (at the room temperature), Fig. 12. There is a difference between the actual Al content in the alloy (3 wt%) and the maximum solid solubility of Al in Mg at the room temperature; hence, the remnant Al enters to the $Mg_{17}Al_{12}$ compound that is formed in the alloy.

At this place it is worth to note that the $Mg_{17}Al_{12}$ phase exists in a relatively wide range of Al contents in binary Mg—Al system, Fig. 12 [34]. The upper Al content corresponds to the stoichiometry Mg_3Al_2 (60 at.%Mg), at the eutectic temperature of 437 °C. Nevertheless, the Al content in the $Mg_{17}Al_{12}$ slightly decreases with temperature; hence, the formation of Mg_3Al_2 is unlikely in magnesium alloys with Al content lower than approx. 12.7 wt% (maximum solid solubility of Al in Mg).

Quan et al. [12] have also pointed out that $Mg_{17}Al_{12}$ particles may appear at grain boundaries (intergranularly) or inside the grains (intragranularly scattered particles). The location of these particles depends mainly on heat input and, thus, on the cooling rate. With decreasing heat input, the cooling rate increases, so most Al atoms cannot diffuse to the grain boundary in time. Therefore, most of the particles are located inside the grains. In the current work, the majority of particles was found to be intragranular because of relatively low heat input, which is in good agreement with the results published by Quan et al. [12].

In the current work it was also observed that the volume fraction of $Mg_{17}Al_{12}$ particles decreases with laser output power, but the inter-particle spacing increases at the same time. This finding is in excellent agreement with the results obtained by Shen et al. [21] who examined the metallurgical consequences of laser welding of the AZ61 alloy. They demonstrated that the higher cooling rate in the welds improved the nucleation of the $Mg_{17}Al_{12}$ particles (but also the α-Mg grains, see discussion above), which may have resulted in a decrease in their inter-particle spacings (or an increase in their number). On the other hand, the size of the $Mg_{17}Al_{12}$ particles is practically independent on the applied welding parameters, suggesting that the differences in cooling rates between each particular weld joints are not enough to be reflected in the differences in particle sizes. Gao et al. [35] have investigated microstructures of hybrid laser MIG welded dissimilar Mg–Al–Zn alloys. They have found much coarser $Mg_{17}Al_{12}$ particles in the MIG-welded parts of

the weld joints as compared with those formed in laser-welded parts. It should be noted, however, that the MIG-welded parts of the joints were much larger than the laser-welded ones, which resulted in considerable differences in cooling rates during solidification.

The presence of very narrow heat-affected zones in laser-welded Mg alloys is a typical feature of applying this technique for the joining of these materials. Coelho et al. [23], for instance, reported a width of the heat-affected zone of 10 μm in the Nd:YAG laser-welded AZ31 alloy. Also, they observed only a slight increase in grain size in HAZ, while a coarsening of $Mg_{17}(Al,Zn)_{12}$ particles has been detected. The increased grain size found in the current work can be due to the high temperature in the close-to-fusion zone region, which may exceed the recrystallization temperature of the alloy [32].

Figure 13a shows an overview bright-field TEM micrograph of the weld metal of the joint made by laser irradiation with an output power of 1.2 kW. First of all, shear bands are clearly visible on the micrograph, suggesting shear deformation of the material inside the grains. In addition, several precipitates are visible; their size ranges between 50 and 200 nm. STEM imaging coupled with EDS analysis Fig. 13b identified significant differences in their chemistry, suggesting their different natures. The particle denoted as "1" is rich in Al and Mn (about 45 wt% Mn, 40 wt% Al, and 15 wt% Mg), while the particle "2" contains around 50 wt%Zn, 40 wt%Mg, and 10 wt%Al, and the particle "3" has 60 wt% Mg, 30 wt%Zn, and 10 wt%Al at the same time. Based on the estimated amounts of the main elements, the probable stoichiometry (in at.%) of these three particles can also be delineated. Of course, the influence of the high magnesium containing matrix should inevitably be taken into the consideration. The particle "1" has an approximate Al + Mg vs. Mn atomic percent ratio of 1.78, which is near to 1.6 typical for $(Al, Mg)_8Mn_5$. This phase may appear in the fusion zones of the given alloy, as reported by Commin et al. [22], for instance, in a form of regularly shaped and around 100 nm-sized particles. Of note, this phase neither occurs in the Al—Mn binary [36] nor in the Al-Mn-Mg ternary equilibrium diagram [37] at a room temperature. However, it can exist at much higher temperatures in both systems. Since the laser welding is a highly non-equilibrium process, a part of the $(Al,Mg)_8Mn_5$ particles can be preserved at room temperature after rapid cooling. The particle "2" manifests a Mg-to-(Zn + Al) atomic percent ratio of approx. 1.45. This is close to the value of 1.42, which is typical for the $Mg_{17}(Al,Zn)_{12}$. The presence of $Mg_{17}(Al,Zn)_{12}$ compound is a typical feature of laser- or electron beam-welded AZ31 (or similar) alloys [22,23,30,38]. Moreover, it seems that the $Mg_{17}(Al,Zn)_{12}$ phase appears in the fusion zones in two variants: The first one is incoherent particles with a size up to 300–500 nm, as demonstrated in Fig. 10, and the second variant is
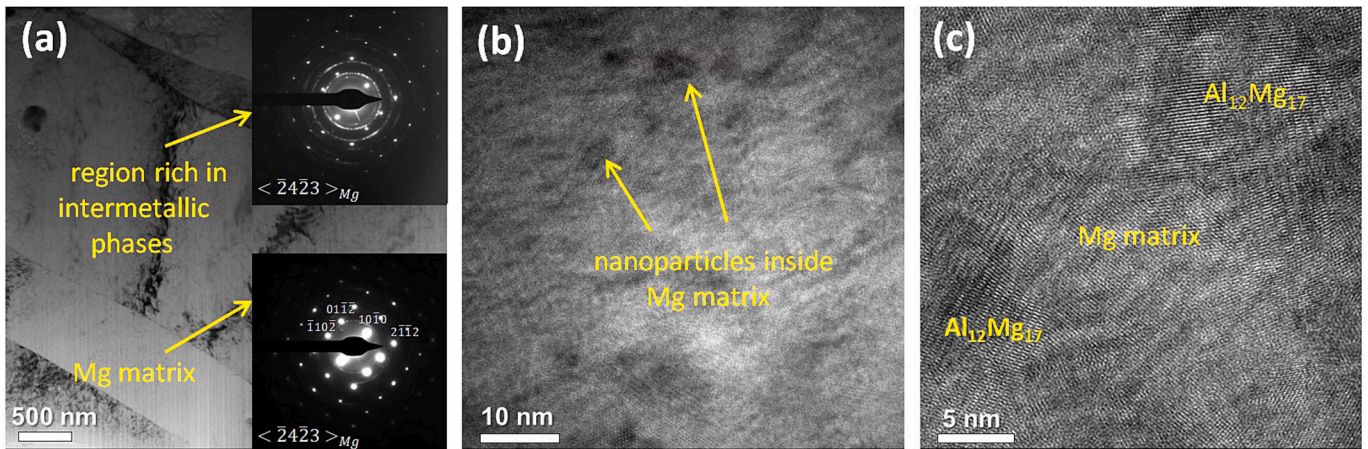
Fig. 14. TEM images of the weld metal in the weld joint made by using a 1.2 kW laser output power. (a) bright-field micrograph; (b) HRTEM micrograph showing nano-sized precipitates inside the matrix; (c) more detailed HRTEM micrograph showing $Mg_{17}Al_{12}$ precipitates.
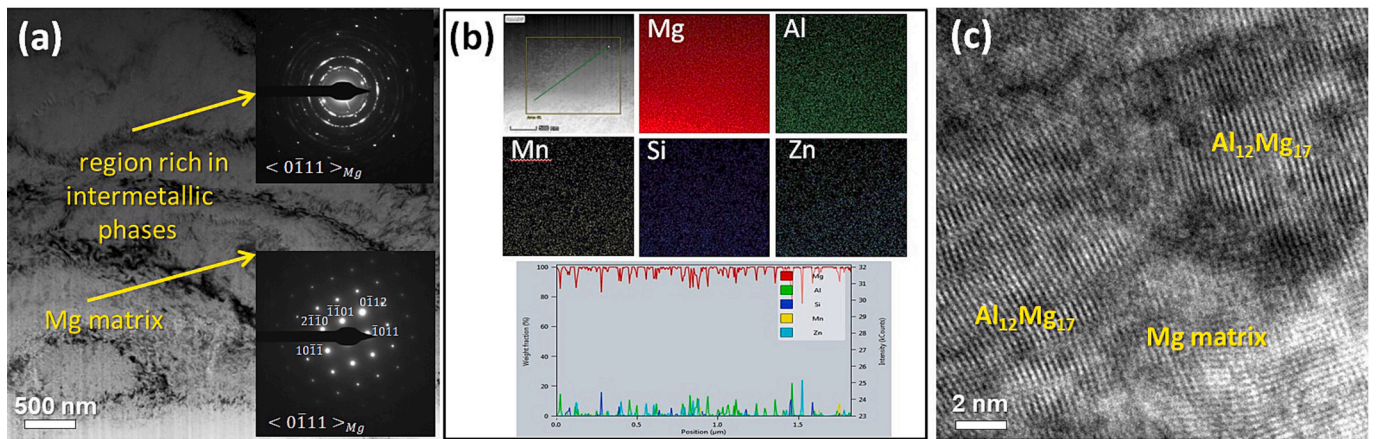

Fig. 15. TEM images of the weld metal in the weld joint made by using a 1.6 kW laser output power (a) bright-field TEM micrograph, (b) EDS maps and elemental line profile throughout the micrograph 15a, and (c) HRTEM image showing $Al_{12}Mg_{17}$ phase in the Mg matrix.
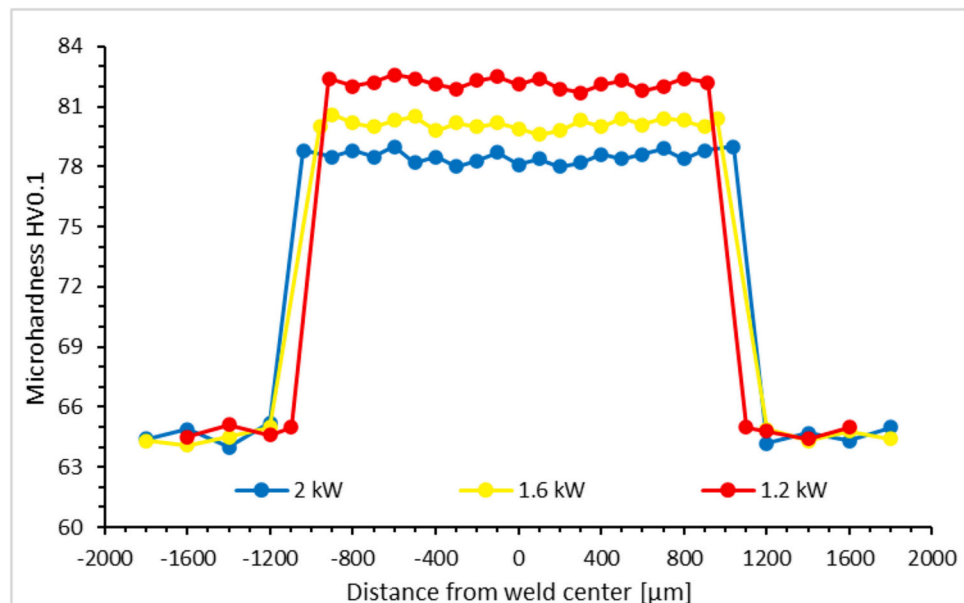

Fig. 16. Typical microhardness profiles across the laser-welded joints at different output power values.

represented by nano-sized coherent particles Figs. 14, 15. The cause of incoherent $Mg_{17}(Al,Zn)_{12}$ particle formation was delineated in the earlier text; briefly, their formation can be ascribed to the difference between the liquid- and solid solubility of Al in Mg and to inhibited diffusion of Al from the interior of grains to the grain boundaries resulting from the rapid solidification. On the other hand, the presence of nano-sized particles may be attributed to their preferential solid-state precipitation at sites with enhanced Mn content, as Tamura et al. pointed out [39]. The source of sites with enhanced Mn content is not clear yet; one can only hypothesise that this may be due to the partial decomposition of $(Al,Mg)_8Mn_5$ during cooling. The particle "3" contains approx. 75 at.% Mg and only 10–15 at.% Zn or Mg. This composition does not match any of the existing phases in Mg—Al or Mg—Zn binary diagrams, due to the much higher Mg content. One can hypothesise that the measurement may be influenced by the high Mg content in the matrix.

The presence of $Mg_{17}(Al,Zn)_{12}$ in laser-welded AZ31 alloy was also confirmed by HRTEM analyses of the obtained weld metal. A bright-field TEM micrograph of the 1.2 kW laser output power-welded sample, Fig. 14a, shows a Mg matrix with a huge number of precipitates inside. Corresponding SAED patterns (in the inset) clearly delineate highly oriented crystalline grains of Mg-matrix (bright spots in patterns), while additional diffraction rings are from different intermetallic phases. Indeed, a large number of nanoparticles of a few nanometres in size are distributed within the matrix, as Fig. 14b illustrates. In fact, the lattice spacings in the nanoparticles are clearly visible in the magnified image, Fig. 14c. The interplanar spacings are estimated to be about 0.218 and 0.215 nm, which match the $Mg_{17}Al_{12}$ phase [40], and the 0.160 nm spacing is typical for hexagonal Mg solid solution [41].

Figure 15a shows a bright field TEM image of the weld metal obtained with 1.6 kW laser power. Also, in this case, the microstructure is composed of the matrix and areas with the presence of a great number of nanosized precipitates. These precipitates are rich in alloying elements, mainly Al and Zn Fig. 15b. In a similar way to the weld metal produced at 1.2 kW laser output power, HRTEM investigations revealed the presence of the $Mg_{17}Al_{12}$ phase within the matrix, Fig. 15c. It should be noted here that the examination of weld metal obtained at 2 kW laser output power gave very similar outcomes.

3.3. Microhardness distribution

From the microhardness distribution across the weld joints and adjacent zones, it is evident that all the fusion zones have a higher microhardness than the base material (~65 HV 0.1). The average values were 78, 80, and 83 HV 0.1 for weld joints made at the output powers of 2, 1.6, and 1.2 kW, respectively, Fig. 16. The higher microhardness of all weld joints as compared with the base material can be attributed to the formation of a supersaturated alpha solid solution along with the enhanced population density of $Mg_{17}Al_{12}$ phase particles. Very consistent results were obtained by many authors after laser- or electron beam welding of different Mg-alloys such as AZ31 [4, 20, 22, 23], AZ61 [20,21], AZ91 [20], or Mg-10Li-3Al-3Zn [17] alloys. In these works, increased microhardness values in weld metals were attributed to various phenomena that take place during the welding heat cycle. These phenomena involve general microstructural refinement, less or more extensive dissolution of $Mg_{17}Al_{12}$ and thus the formation of supersaturated solutions, and refinement of precipitates (in the case of Mg-10Li-3Al-3Zn [17]). Decreasing the laser output power produces slightly higher microhardness inside the fusion zones. As evident from Figs. 5 and 6, lower laser output power produces smaller weld joints. One can this expert faster heating/cooling cycles in these cases. This may, for instance, further increase the supersaturation of solid solution and microstructural refinement. Quantitative microstructural analyses revealed a decrease in both the grain size and the interparticle spacings of $Mg_{17}Al_{12}$ with decreasing the laser output power, which is consistent with the last consideration. Similar observations were obtained by Wang

Table 6
Effect of laser output power on the tensile properties of laser welded AZ31 alloy.

Laser output power [kW]	UTS [MPa]	YS [MPa]	Joint efficiency [%]
1.2	226	164	89.3
1.6	203	126	80.2
2	176	119	69.6

et al. [4] for laser-welded AZ31 alloy and by Shen et al. [21] for laser-welded AZ61 alloy. As the main source of increased hardness obtained in weld joints produced at lower output power, more extensive microstructural refinement (Hall-Petch strengthening) was considered.

3.4. Tensile testing and fractography

The results of the tensile tests are listed in Table 6. The ultimate tensile strength (UTS) approaches that of the unwelded base metal in the case of 1.2 kW laser output power, and the joint efficiency is close to 90%. However, increasing the laser output power to either 1.6 or 2 kW reduced both the UTS and YS and produced lower joint efficiency. There are only a few papers that have in-depth examined the mechanical properties of weld joints made on different AZ-class alloys. In one of them, Shen et al. [17] have established a decreasing UTS from 268 to 143 MPa with a decreasing laser welding speed from 2800 to 1800 mm. min^{-1} for laser welding of AZ61 alloy. Very consistent results were achieved by Chowdhury et al. [14] for fiber laser-welded AZ31 material. Of note, any decrease in laser welding speed results in a larger weld bath, thus in a slower heating /cooling cycle. This may be reflected, for instance, in coarser internal weld joint microstructure and lower solid solution supersaturation. In the current work, variations in heat input were obtained by changes in laser output power. It has been determined that higher laser output power produces a coarser microstructure than what is obtained by lower output power. The variations in mechanical properties of weld joints, Table 6, can be considered logical.

Figure 17 is a compilation of overview SEM images of fracture surfaces for weld joints prepared by different laser output powers. All the fracture surfaces feature more or less equi-axed dimples together with cleavage facettes, suggesting a mixed ductile/brittle fracture behaviour. Similar appearances of fracture surfaces after tensile tests were also obtained by other authors [14,17,21,30,32]. It is worth noting that the tensile testing in the current work as well as in the cited papers was conducted at very slow strain rates at the room temperature. Slow strain rates usually promote the creation of ductile fractures. However, magnesium and its alloys crystallize in a hexagonal close-packed structure and the number of slip systems is therefore limited at room temperature. Detailed SEM images, Fig. 18, with particular emphasis on the initiation of ductile dimples, clearly delineate that the dimples are a result of a decohesive initiation at intermetallic particle/matrix interfaces. The more $Mg_{17}Al_{12}$ particles present in the microstructure, the higher is the probability of ductile fracture initiation and propagation. Quantitative assessment of $Mg_{17}Al_{12}$ particles revealed their highest volume fraction and correspondingly lowest interparticle spacing in the weld joint made at 1.2 kW output power. This may be one of the possible sources of the best UTS for this particular weld joint.

3.5. Confirmation calculations

The increase in UTS and YS can be attributed to grain refinement, variations in dissolved alloying elements in the matrix, and the changes in quantitative characteristics of the minor $Mg_{17}Al_{12}$ phase. Based on the measured/calculated microstructural parameters (see Table 5), the magnitudes of individual contributions can be estimated.

3.6. Solid solution strengthening

The AZ31 alloy contains two main alloying elements: aluminium and
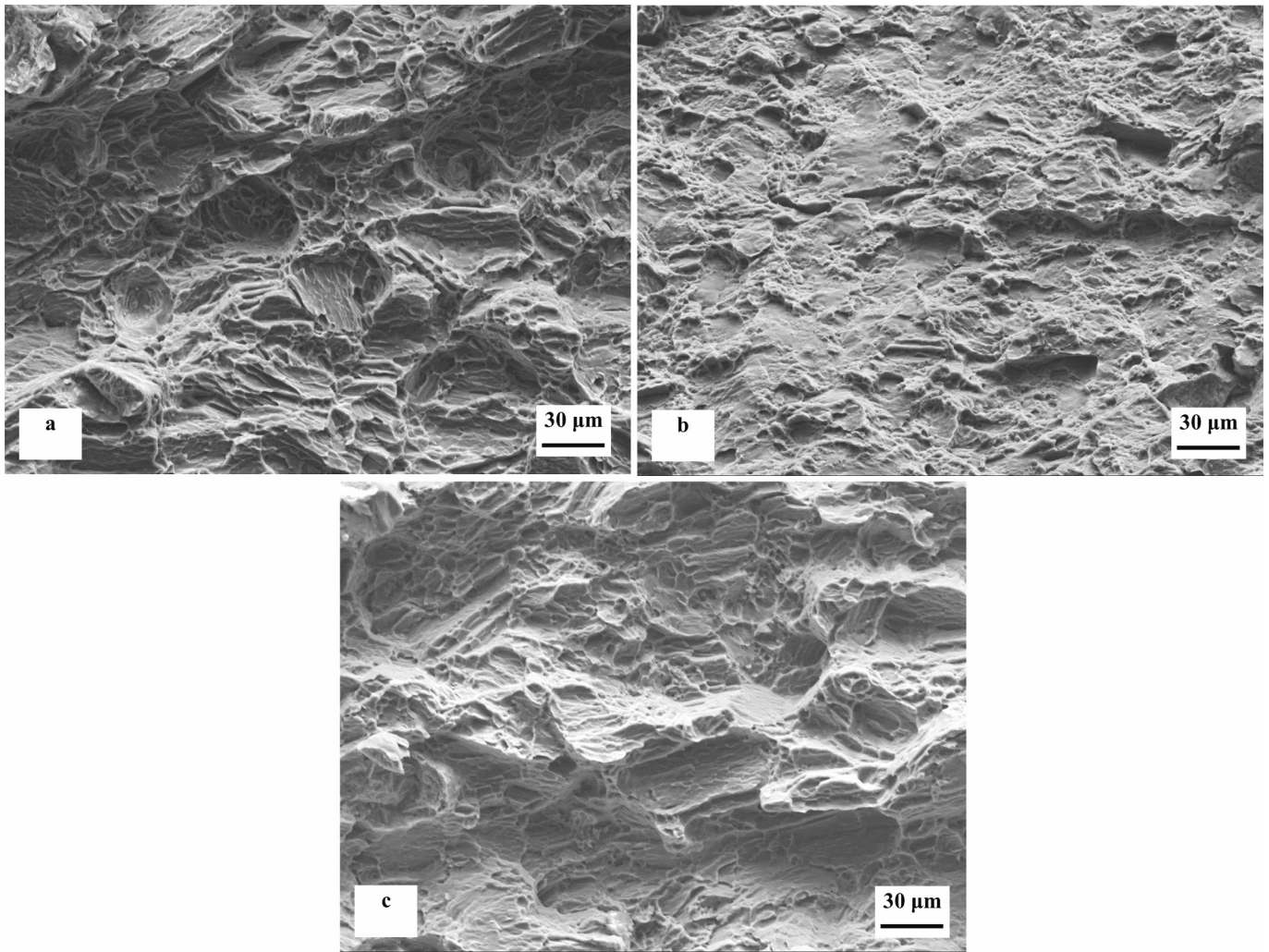
Fig. 17. Typical overview SEM images showing the fracture surfaces after tensile testing of the weld joints prepared at the output power of (a) 1.2 kW, (b) 1.6 kW, and (c) 2 kW.

zinc. These elements form a substitutional solid solution with magnesium. As compared with the base material, the aluminium content in the weld joint is influenced only slightly by the welding process. Contrarily, zinc content is slightly reduced since zinc is evaporated much more easily during welding. The effect of solid solution strengthening may be given by Eq. 4 [42]:

$$YS_{ss} = X \times C^{2/3} \tag{4}$$

where X is a constant (197 MPa $\times$ C$^{-2/3}$, according to [42]), and C is the concentration of the given solute (at.%).

3.7. Grain boundary strengthening

The effect of grain size on the yield strength can be estimated by the well-known Hall-Petch relation, which is given by Eq. 5 [43]:

$$YS_{GB} = \sigma_o + k \times d^{-1/2} \tag{5}$$

where σ_o is the constant (called also „lattice intrinsic resistance to dislocation movement", it is 11 MPa [44]), k is a constant that characterizes the relative strengthening caused by grain boundaries (according to Gao et al. [45], the k = 164 MPa $\times$ μm$^{1/2}$), and d is the grain diameter.

3.8. Precipitation strengthening

Laser welding is a highly non-equilibrium process as it induces high heating and cooling rates in welded materials. When the magnesium alloy AZ61 was laser-welded, for instance, the cooling rates during the solidification of molten metal ranged between 1 and 2×10^4 Ks^{-1} [21]. For the AZ31 alloy, a high cooling rate results in a substantially increased amount and population density of minor Mg$_{17}$Al$_{12}$ particles formed in the fusion zones, Figs. 9, 10. The interfaces between the matrix and Mg$_{17}$Al$_{12}$ particles are incoherent since these phases are different in their crystal structures and lattice parameters. Therefore, the total magnitude of strengthening can be divided into four partial contributions, namely: a) the Orowan process, which is defined as an interaction between dislocations and incoherent particles; b) the load transfer from a matrix to Mg$_{17}$Al$_{12}$ particles; c) the contribution given by the generation of new dislocations, which results from differences in thermal expansion between the matrix and Mg$_{17}$Al$_{12}$ particles; and d) the geometrical incompatibility between a matrix and Mg$_{17}$Al$_{12}$ particles that also causes the formation of geometrically necessary dislocations.

a) Orowan process. For spherical or almost fully regular-shaped particles, Figs. 9, 10a, the yield stress increment can be expressed by Eq. 6 [42]:
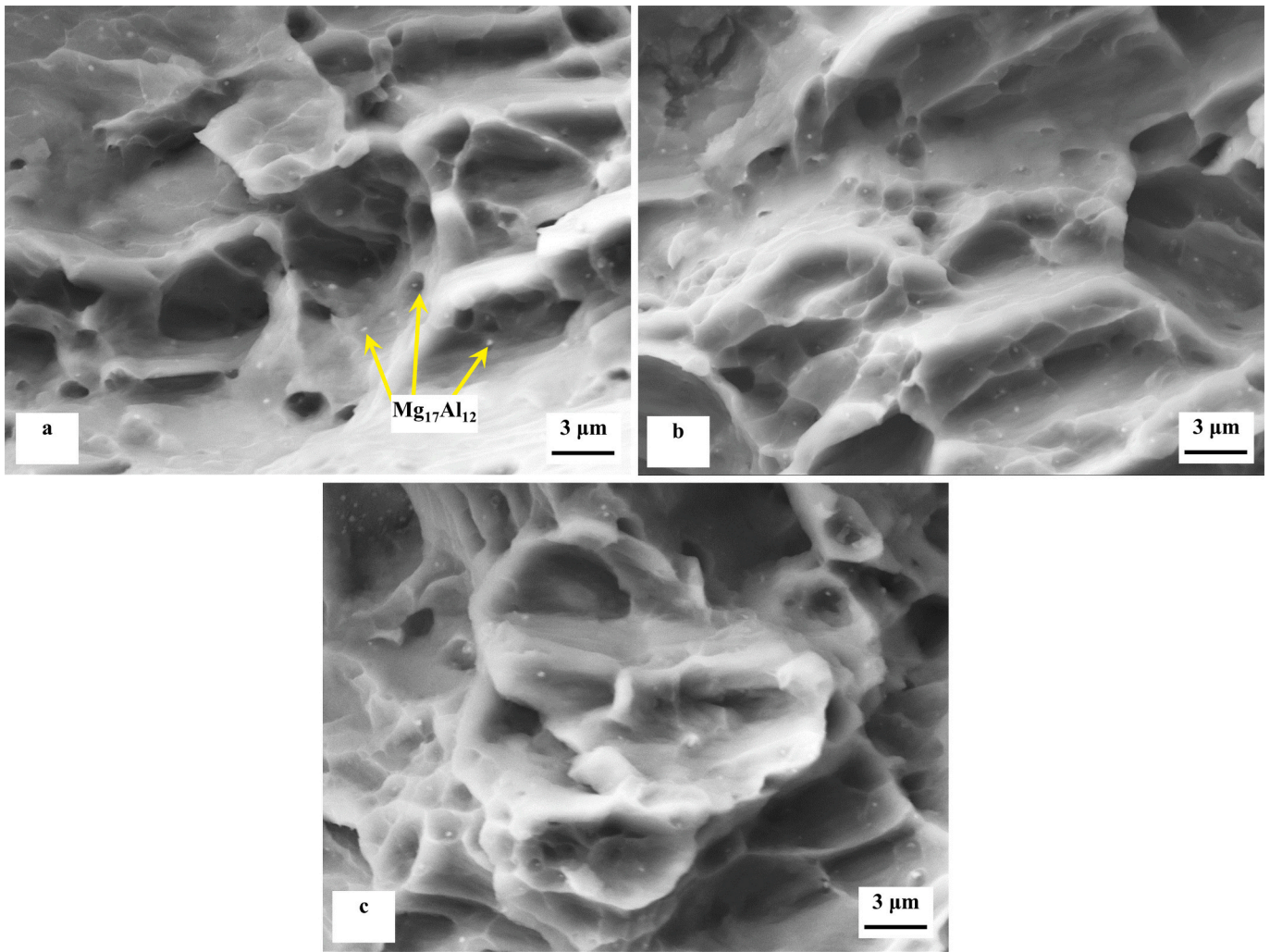
Fig. 18. Detailed SEM images showing the fracture surfaces after tensile testing of the weld joints prepared at the output power of (a) 1.2 kW, (b) 1.6 kW, and (c) 2 kW.

$$YS_{OR} = \frac{M \times G \times b}{2 \times \pi \times \sqrt{1-\upsilon}} \times \frac{1}{\lambda} \times ln\left(\frac{d_t}{r_o}\right) \qquad (6)$$

where M is the Taylor factor (considered to be 5), G is the shear modulus of the matrix (determined to be 17×10^3 MPa), b is the magnitude of burgers vector for Mg (3.2×10^{-10} m, according to [44]), υ is the Poisson number, λ is the interparticle spacing of $Mg_{17}Al_{12}$ particles, r_o is equal to b, and d_t is the mean diameter of $Mg_{17}Al_{12}$ particles.

b) Generation of new dislocations due to differences in thermal expansion.

New dislocations are generated through the effects caused by different thermal expansivities of the matrix and intermetallics. This may make a substantial contribution to the total yield strength and can be expressed by Eq. 7 [46]:

$$YS_{TE} = \alpha \times G \times b \times \left(\frac{12 \times \Delta T \times \Delta C \times f}{b \times d_t}\right)^{1/2} \qquad (7)$$

where G is the shear modulus of the matrix, α is a constant (1.25, according to [46]), b is the magnitude of burgers vector for Mg, ΔT is the difference between the solidus line temperature of the alloy (estimated to be 833 K, based on the data published in [42]) and the room temperature, ΔC is the difference between thermal expansion coefficients of

the matrix (3.2×10^{-5} K^{-1} [47]) and $Mg_{17}Al_{12}$ (7.5×10^{-6} K^{-1} [46]), f is the volume fraction of $Mg_{17}Al_{12}$, and d_t is the mean diameter of $Mg_{17}Al_{12}$ particles.

c) Load transfer.

During the plastic deformation, load is transferred from the matrix to the minor-phase particles. The $Mg_{17}Al_{12}$ particles are mostly regularly shaped, Fig. 10. Therefore, the strengthening contribution can be quantitatively estimated using Eq. 8 [46]:

$$YS_{LT} = \sigma_m \times \frac{f}{2} \qquad (8)$$

where σ_m is the yield strength of the matrix (this value can be considered equal to YS_{ss}) and f is the volume fraction of $Mg_{17}Al_{12}$.

d) New dislocation formed due to geometrical incompatibility.

SEM images in Fig. 10 show that a great number of $Mg_{17}Al_{12}$ particles are generated in fusion zones. They are incompatible with the matrix; thus, the generation of geometrically necessary dislocations during deformation is caused. The contribution of this phenomenon can be given by Eq. 9:

Table 7

Contributions to the total yield strength value [MPa] of the weld joints are calculated from microstructural characteristics. YS_{SS}: solid solution strengthening; YS_{GB}: grain boundary strengthening; YS_{OR}: Orowan process; YS_{TE}: generation of new dislocation due to differences in thermal expansion; YS_{LT}: load transfer; YS_{GEO}: new dislocation formed due to geometrical incompatibility.

Laser output power [kW]	YS_{SS} [MPa]		YS_{GB} [MPa]	Precipitation strengthening				Calculated YS [MPa]
	Al	Zn		YS_{OR} [MPa]	YS_{TE} [MPa]	YS_{LT} [MPa]	YS_{GEO} [MPa]	
1.2	16	4.3	47.2	20.4	39	0.37	32	159.27
1.6	19.8	4.2	42.9	17.7	32	0.28	26	142.88
2	17.7	3.8	41.1	16.5	29	0.21	23	131.31
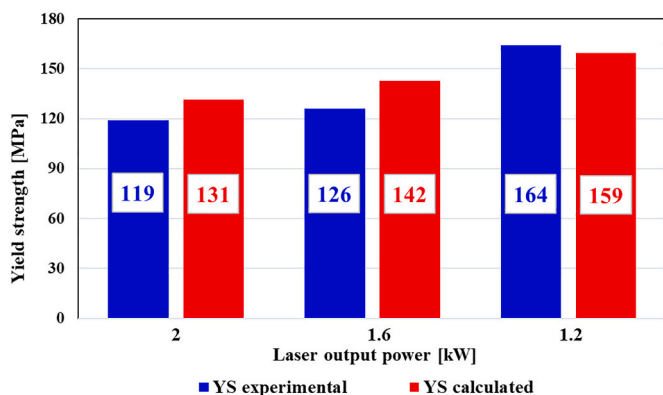
Fig. 19. Comparison of experimentally determined yield strength values with calculated ones.

$$YS_{GEO} = \alpha \times G \times b \times \left(\frac{8 \times \gamma \times f}{b \times d_t} \right)^{1/2} \qquad (9)$$

where G is the shear modulus of the matrix, α is a constant (1.25, according to [46]), b is the magnitude of the burgers vector for Mg, γ is the shear strain (0.013, according to [21]), f is the volume fraction of $Mg_{17}Al_{12}$, and d_t is the mean diameter of $Mg_{17}Al_{12}$ particles.

From Table 7, it shows that the effect of most strengthening mechanisms increases with a decrease in laser output power (or decrease in heat input). The highest contribution to the final yield strength value is from the grain boundary strengthening. But the contributions from the precipitation strengthening also play an important role. The lower than expected contribution of solid solution strengthening in the case of 1.2 kW laser output power may be due to the considerably increased amount of $Mg_{17}Al_{12}$ particles formed in this particular weld joint. These particles need a much higher amount of aluminium for their formation; hence, the solid solution is logically depleted by Al. By comparing the calculated yield strength magnitudes with the ones determined by tensile testing, Fig. 19 it is shown that they are in excellent agreement (difference max. 12% in the case of 1.6 kW laser power). This may be mainly due to the low defect density (like pores) of the weld joints, see Fig. 7. The assumption that the obtained values of mechanical properties characterize the welded material only is correct.

4. Conclusions

In this study, the effect of laser beam power on the microstructure and mechanical properties of AZ31B magnesium alloy weld joints were investigated. The following main conclusions could be drawn:

- All the weld joints produced at laser output power in the range of 1.2–2 kW are almost defect-free.
- The microstructures of the weld joints contain columnar grains oriented perpendicularly to the fusion zone-base metal interface and equi-axed grains in the centres of the welds. The minor phase is

$Mg_{17}Al_{12}$; however, the weld joints also contain different nano-sized precipitates like $Mg_{17}Al_{12}$ or $(Al,Mg)_8Mn_5$.
- The obtained as-welded microstructures are refined as compared with the base metal. The extent of microstructural refinement increases with decreasing laser output power.
- Weld joints manifest elevated microhardness values as compared with the base metal. The highest microhardness (83 HV 0.1) is achieved by using the lowest laser output power.
- The ultimate tensile strength of the weld joints is lower than that of the base metal; the highest values were produced by 1.2 kW laser output power. The use of higher laser output power resulted in a decrease in ultimate tensile strength. The same applies for yield strength. The obtained yield strength values are in very good agreement with the calculated ones, with a maximum difference of 12%. This indicated that the measured values of mechanical properties are almost not influenced by the imperfections of weld joints and represent the welded material only.

CRediT authorship contribution statement

Maroš Vyskoč: Data curation, Investigation, Visualization. **Mirjana Novaković:** Data curation, Formal analysis, Investigation, Validation. **Jelena Potočnik:** Investigation, Methodology. **Pavel Kovačocy:** Data curation, Formal analysis, Investigation. **Peter Jurči:** Conceptualization, Methodology, Supervision, Writing – original draft, Writing – review & editing.

Declaration of competing interest

The authors declare that they have no known competing financial interests or personal relationships that could have appeared to influence the work reported in this paper.

Data availability

Data will be made available on request.

References

[1] Y. Yang, X. Xiong, J. Chen, X. Peng, D. Chen, F. Pan, Research advances in magnesium and magnesium alloys worldwide in 2020, J. Magnes. Alloy. 9 (2021) 705–747, https://doi.org/10.1016/j.jma.2021.04.001.
[2] V. Balajiad, V. Bupesh Rajaa, K. Palanikumarb, Ponshanmugakumarc N. Adityaa, V. Rohita, Effect of heat treatment on magnesium alloys used in automotive

industry: a review, Mater. Today: Proceed. (2021), https://doi.org/10.1016/j.matpr.2021.02.017.

[3] M. Rakshith, P. Seenuvasaperumal, Review on the effect of different processing techniques on the microstructure and mechanical behaviour of AZ31 magnesium alloy, J. Magnes. Alloy. 9 (2021) 1692–1714, https://doi.org/10.1016/j.jma.2021.03.019.

[4] Z. Wang, M. Gao, H. Tang, X. Zeng, Characterization of AZ31B wrought magnesium alloy joints welded by high power fiber laser, Mater. Charact. 62 (2011) 943–951, https://doi.org/10.1016/j.matchar.2011.07.002.

[5] X. Cao, M. Jahazi, J. Immarigeon, W. Wallace, A review of laser welding techniques for magnesium alloys, J. Mater. Process. Technol. 171 (2006) 188–204, https://doi.org/10.1016/j.jmatprotec.2005.06.068.

[6] X. Nan, Ch. Lu, L. Chen, W. Sun, H. Yu, L. Liu, K. Chen, Zh. Xiong, Zh. Gao, J. Li, Preparation of laminated structure in AZ31 magnesium alloy by explosive welding, Mater. Lett. 268 (2020) 127574, https://doi.org/10.1016/j.matlet.2020.127574.

[7] J. Zhu, L. Li, Z. Liu, CO_2 and diode laser welding of AZ31 magnesium alloy, Appl. Surf. Sci. 247 (2005) 300–306, https://doi.org/10.1016/j.apsusc.2005.01.162.

[8] H. Haferkamp, M. Niemeyer, U. Dilthey, G. Trager, Laser and electron beam welding of magnesium materials, Mater. Werkst. 30 (1999) 682–692. DOI: 10.1002/(SICI)1521-4052(199911)30:11<682::AID-MAWE682>3.3.CO;2–0.

[9] E. Aghion, B. Bronfin, Magnesium alloys development towards the 21st century, Mater. Sci. Forum 350–351 (2000) 19–28, https://doi.org/10.4028/www.scientific.net/MSF.350-351.19.

[10] M. Pastor, H. Zhao, T. DebRoy, Continuous wave-Nd:yttrium–aluminium–garnet laser welding of AM60B magnesium alloys, J. Laser Appl. 12 (2000) 91–100, https://doi.org/10.2351/1.521922.

[11] J. Wegrzyn, M. Mazur, A. Szymański, B. Balcerowska, Development of a filler for welding magnesium alloy GA8, Weld. Int. 1 (2010) 146–150, https://doi.org/10.1080/09507118709452102.

[12] Y. Quan, Z. Chen, X. Gong, Z. Yu, Effects of heat input on microstructure and tensile properties of laser welded magnesium alloy AZ31, Mater. Charact. 59 (2008) 1491–1497, https://doi.org/10.1016/j.matchar.2008.01.010.

[13] M. Gao, H. Wang, K. Hao, H. Mu, X. Zeng, Evolutions in microstructure and mechanical properties of laser lap welded AZ31 magnesium alloy via beam oscillation, J. Manuf. Process. 45 (2019) 92–99, https://doi.org/10.1016/j.jmapro.2019.07.001.

[14] S. Chowdhury, D. Chen, S. Bhole, E. Powidajko, D. Weckman, Y. Zhou, Fiber laser welded AZ31 magnesium alloy: the effect of welding speed on microstructure and mechanical properties, Metall. Mater. Trans. A43 (2012) 2133–2147, https://doi.org/10.1007/s11661-011-1042-z.

[15] K. Hao, H. Wang, M. Gao, R. Wu, X. Zeng, Laser welding of AZ31B magnesium alloy with beam oscillation, J. Mater. Res. Technol. 8 (2019) 3044–3053, https://doi.org/10.1016/j.jmrt.2019.04.024.

[16] X. Zhang, Z. Cao, Effects of pulse shaping on Nd:YAG laser spot welds in an AZ31 magnesium alloy, Opt. Lasers Eng. 119 (2019) 1–8, https://doi.org/10.1016/j.optlaseng.2019.02.002.

[17] L.J. Zhang, H.B. Zhang, X.W. Lei, R. Wang, B.F. Han, J.X. Zhang, S.J. Na, Laser processing of Mg-10Li-3Al-3Zn alloy: Part I – Microstructure and properties of laser welded joints, J. Manuf. Process. 57 (2020) 871–880, https://doi.org/10.1016/j.jmapro.2020.07.053.

[18] S. Niknejad, L. Liu, M. Lee, Sh. Esmaeili, N. Zhou, Resistance spot welding of AZ series magnesium alloys: effects of aluminum content on microstructure and mechanical properties, Mater. Sci. Eng. A 618 (2014) 323–334, https://doi.org/10.1016/j.msea.2014.08.013.

[19] Z. Lei, J. Bi, P. Li, T. Guo, Y. Zhao, D. Zhang, Analysis on welding characteristics of ultrasonic assisted laser welding of AZ31B magnesium alloy, Opt. Laser Technol. 105 (2018) 15–22, https://doi.org/10.1016/j.optlastec.2018.02.050.

[20] S.F. Su, J.C. Huang, H.K. Lin, N.J. Ho, Electron-beam welding behavior in Mg-Al–based alloys, Metall. Mater. Trans. A A33 (2002) 1461–1473, https://doi.org/10.1007/s11661-002-0069-6.

[21] J. Shen, L. Wen, Y. Li, D. Min, Effects of welding speed on the microstructures and mechanical properties of laser welded AZ61 magnesium alloy joints, Mater. Sci. Eng. A 578 (2013) 303–309, https://doi.org/10.1016/j.msea.2013.04.093.

[22] L. Commin, M. Dumont, R. Rotinat, F. Pierron, J. Masse, L. Barrallier, Texture evolution in Nd:YAG-laser welds of AZ31 magnesium alloy hot rolled sheets and its influence on mechanical properties, Mater. Sci. Eng. A 528 (2011) 2049–2055, https://doi.org/10.1016/j.msea.2010.11.061.

[23] R. Coelho, A. Kostka, H. Pinto, S. Riekehr, M. Kocak, A. Pyzalla, Microstructure and mechanical properties of magnesium alloy AZ31B laser beam welds, Mater. Sci. Eng. A 485 (2008) 20–30, https://doi.org/10.1016/j.msea.2007.07.073.

[24] M. Vyskoč. Influence of Shielding Gas on Weldability of Non-ferrous Metals by Laser. n.d. [Dissertation thesis].

[25] M. Martinkovic, Quantitative Structural Analysis of Materials, 1st ed., STU Bratislava, Slovakia, 2011 (in Czech).

[26] G. Song, Z. Diao, X. Lv, L. Liu, TIG and laser–TIG hybrid filler wire welding of casting and wrought dissimilar magnesium alloy, J. Manuf. Process. 34 (2018) 204–214, https://doi.org/10.1016/j.jmapro.2018.06.005.

[27] N. Bailey, W. Tan, Y. Shin, A parametric study on laser welding of magnesium alloy AZ31 by a Fiber Laser, J. Manuf. Sci. Eng. 137 (2015) 1–9, https://doi.org/10.1115/1.4029052.

[28] H. Liu, J. Zhou, Y. Chen, T. Li, X. Jiao, Y. Yang, T. Lin, K. Cheng, Characterization of AZ31B magnesium alloy joints welded with a Nd:YAG Laser, Mater. Technol. 52 (2018) 487–492, https://doi.org/10.17222/mit.2017.180.

[29] M. Zhang, J. Wu, C. Mao, B. Cheng, H.M.D. Shakhawat, H. Li, K. Wang, J. Zhang, Y. Hu, Z. Bi, Impact of power modulation on weld appearance and mechanical properties during laser welding of AZ31B magnesium alloy, Opt. Laser Technol. 156 (2022) 108490, https://doi.org/10.1016/j.optlastec.2022.108490.

[30] C. Jinqiu, L. Fei, W. Zhisheng, L. Weigang, Effect of heat input on the microstructure and mechanical properties of an electron-beam-welded AZ31 magnesium alloy, Mater. Technol. 54 (2020) 819–828, https://doi.org/10.17222/mit.2020.073.

[31] M. Zimina, P. Málek, J. Bohlen, D. Letzig, G. Kurz, M. Cieslar, Mechanical properties of homogenized twin-roll cast and conventionally cast AZ31 magnesium alloys, Mater. Eng. - Mater. Inžinierst. 22 (2015) 8–15.

[32] S.M. Chowdhury, D.L. Chen, S.D. Bhole, E. Powidajko, D.C. Weckman, Y. Zhou, Microstructure and mechanical properties of Fiber-Laser-welded and diode-laser-welded AZ31 magnesium alloy, Metall. Mater. Trans. A 42A (2011) 1974–1989, https://doi.org/10.1007/s11661-010-0574-y.

[33] R. Mola, A. Dziadoń, Formation of magnesium-eutectic mixture layered composite, Arch. Foundry Eng. 8 (2008) 127–132.

[34] J.L. Murray, The Al-Mg (aluminum-magnesium) system, Bull. Alloy Phase Diagr. 3 (1982) 60–74.

[35] M. Gao, Y. Cao, X.Y. Zeng, T.X. Lin, Mechanical properties and microstructures of hybrid laser MIG welded dissimilar Mg–Al–Zn alloys, Sci. Technol. Weld. Join. 15 (2010) 638–645, https://doi.org/10.1179/136217110X12813393169697.

[36] T. Laser, M.R. Nürnberg, A. Janz, Ch. Hartig, D. Letzig, R. Schmid-Fetzer, R. Bormann, The influence of manganese on the microstructure and mechanical properties of AZ31 gravity die cast alloys, Acta Mater. 54 (2006) 3033–3041, https://doi.org/10.1016/j.actamat.2006.02.039.

[37] V. Raghavan, Al-Mg-Mn (Aluminum-Magnesium-Manganese), J. Phase Equilib. Diffus. 31 (2010) 46, https://doi.org/10.1007/s11669-009-9621-z.

[38] H.T. Liu, J.X. Zhou, D.Q. Zhao, Y.T. Liu, J.H. Wu, Y.S. Yang, B.Ch. Ma, H. H. Zhuang, Characteristics of AZ31 mg alloy joint using automatic TIG welding, Int. J. Miner. Metall. Mater. 24 (2017) 102–108, https://doi.org/10.1007/s12613-017-1383-8.

[39] Y. Tamura, Y. Kida, A. Suzuki, H. Soda, A. McLean, Effects of solute segregation on precipitation phenomena and age hardening response of high-purity and commercial AZ91 magnesium alloy, Mater. Trans. 50 (2009) 579–587, https://doi.org/10.2320/matertrans.MRA2008381.

[40] N. Wang, W.Y. Yu, B.Y. Tang, L.M. Peng, W.J. Ding, Structural and mechanical properties of Mg17Al12 and Mg24Y5 from first-principles calculations, J. Phys. D. Appl. Phys. 41 (2008) 195408, https://doi.org/10.1088/0022-3727/41/19/195408.

[41] H.E. Swanson, E. Tatge, Standard X-ray diffraction powder patterns, National Bureau of standards (U.S.), Circular 539 (359) (1953) I1.

[42] C.R. Hutchinson, J.F. Nie, S. Gorsse, Modelling the precipitation processes and strengthening mechanisms in a Mg-Al-(Zn) AZ91 alloy, Metall, Mater. Trans. 36A (2005) 2093–2105, https://doi.org/10.1007/s11661-005-0330-x.

[43] N. Hansen, Hall-Petch relation and boundary strengthening, Scr. Mater. 51 (2004) 801–806, https://doi.org/10.1016/j.scriptamat.2004.06.002.

[44] S.M. He, X.Q. Zeng, L.M. Peng, X. Gao, J.F. Nie, W.J. Ding, Microstructure and strengthening mechanism of high strength Mg–10Gd–2Y–0.5Zr alloy, J. Alloys Compd. 427 (2007) 316–323, https://doi.org/10.1016/j.jallcom.2006.03.015.

[45] L. Gao, R.S. Chen, E.H. Han, Microstructural and strengthening mechanisms of a cast Mg-1.48Gd-1.13Y-0.16Zr (at.%) alloy, J. Mater. Sci. 44 (2009) 4443–4454, https://doi.org/10.1007/s10853-009-3672-8.

[46] M. Mabuchi, K. Higashi, Strengthening mechanisms of Mg-Si alloys, Acta Mater. 44 (1996) 4611–4618, https://doi.org/10.1016/1359-6454(96)00072-9.

[47] S.L. Shang, Z.K. Liu, in: Mihriban O. Pekguleryuz, Karl U. Kainer, A. Arslan Kaya (Eds.), In: Fundamentals of Magnesium Alloy Metallurgy, Woodhead Publishing Limited, 2013, p. 382.